Modeled O_2 nightglow distributions in the Venusian atmosphere

Marie-Ève Gagné,[1,2] Stella M. L. Melo,[1] Amanda S. Brecht,[3] Stephen W. Bougher,[4] and Kimberly Strong[2]

Received 11 April 2012; revised 12 October 2012; accepted 14 October 2012; published 12 December 2012.

[1] In this paper, we study the global distribution of the O_2 Infrared Atmospheric (0-0) emission at 1.27 μm in the Venusian atmosphere with an airglow model in combination with atmospheric conditions provided by a three-dimensional model, the Venus Thermospheric Global Circulation Model. We compare our model simulations with airglow observations of this emission from the Visible and InfraRed Thermal Imaging Spectrometer on board the Venus Express orbiter. Our model is successful in reproducing the latitudinal and temporal trends seen in the observations for latitudes between 0° and 30°, while poleward of 30°, the model results start to diverge away from the measurements. We attribute this discrepancy to the atomic oxygen distribution at these latitudes in our model that is inconsistent with the recent measurements. We also conducted a sensitivity study to explore the dependence of the vertical structure and the distribution of the airglow emission on the atmospheric conditions. The sensitivity study confirms that changes in the distribution of atomic oxygen significantly affect the characteristics of the airglow layer. Therefore, meaningful comparisons with observations require a three-dimensional model, which accounts for dynamical variations in the background atmosphere. With this investigation, we highlight the impact of the atmospheric conditions on the airglow distribution, which is important for the understanding of how the phenomenon plays.

Citation: Gagné, M.-È., S. M. L. Melo, A. S. Brecht, S. W. Bougher, K. Strong (2012), Modeled O_2 nightglow distributions in the Venusian atmosphere, *J. Geophys. Res.*, *117*, E12002, doi:10.1029/2012JE004102.

1. Introduction

[2] Diagnosis of the airglow mechanisms in the Venusian atmosphere remains an intriguing challenge. Recent measurements are now available for analysis using three-dimensional (3-D) Global Circulation Models (GCMs), providing an opportunity to improve our knowledge of the chemical kinetics that give rise to airglow features. This will enable the use of airglow measurements to infer the distribution of temperature, atomic oxygen density, and other dynamical variables in the neutral atmosphere [*Bougher et al.*, 2006; *Brecht et al.*, 2011; *Bougher et al.*, 2012; *Hoshino et al.*, 2012], and therefore contribute to a better understanding of the atmospheric region below 120 km.

[3] In the Venus nightglow, the Infrared Atmospheric emission at 1.27 μm ($a^1\Delta_g,0 - X^3\Sigma_g^-,0$) is the strongest of all O_2 emissions, with an average maximum intensity of the order of a few megarayleighs (MR). This emission has been observed on several occasions from Earth-based observatories [*Connes et al.*, 1979; *Crisp et al.*, 1996; *Ohtsuki et al.*, 2005, 2008; *Bailey et al.*, 2008; *Krasnopolsky*, 2010] and from space-based instruments [*Bougher and Borucki*, 1994; *Hueso et al.*, 2008; *Gérard et al.*, 2008b, 2009a, 2009b, 2010, 2012; *Piccioni et al.*, 2009; *Shakun et al.*, 2010; *Soret et al.*, 2011; *Migliorini et al.*, 2011]. The source of this emission is oxygen atoms produced during daytime, mainly by photodissociation of CO_2 followed by three-body recombination of these atoms at nighttime, resulting in an airglow emission [*Connes et al.*, 1979]. The nadir and limb observations of the O_2 1.27-μm emission by VIRTIS, the Visible and InfraRed Thermal Imaging Spectrometer on board the Venus Express (VEx) mission, show that the volume emission rate typically peaks between 95 and 100 km. Further, there is a region of maximum emission intensity of 1.2 MR on the equator around midnight [*Gérard et al.*, 2008b, 2009a, 2010, 2012; *Hueso et al.*, 2008; *García Muñoz et al.*, 2009; *Piccioni et al.*, 2009; *Shakun et al.*, 2010; *Soret et al.*, 2011; *Migliorini et al.*, 2011]. *Piccioni et al.* [2009] reported that the total vertical emission rate decreases from 1.15 MR at the equator to 0.2 MR at 70°N. The peak altitude is rather constant, located between 97–99 km, from 0° to 55°N; then it starts to slowly decrease with

[1]Space Science and Technology, Canadian Space Agency, Saint-Hubert, Quebec, Canada.
[2]Department of Physics, University of Toronto, Toronto, Ontario, Canada.
[3]Planetary System Branch, NASA Ames Research Center, Moffett Field, California, USA.
[4]Department of Atmospheric, Oceanic and Space Sciences, University of Michigan, Ann Arbor, Michigan, USA.

Corresponding author: M.-È. Gagné, Space Science and Technology, Canadian Space Agency, Saint-Hubert, QC J3Y 8Y9, Canada. (megagne@atmosp.physics.utoronto.ca)

increasing latitude. Similarly, *Soret et al.* [2011] analyzed the VIRTIS nadir measurements and concluded that the emission has a maximum intensity of ~1.6 MR near the antisolar point close to the midnight meridian, and a mean hemispheric average of 0.47 MR. In this data set, the intensity profiles put the peak altitude between 94 and 99 km.

[4] In many instances, the latitudinal variations of the O_2 IR emission intensity show some localized maxima at higher latitudes, as reported in the literature [*Hueso et al.*, 2008; *Gérard et al.*, 2009b, 2012; *Piccioni et al.*, 2009; *Shakun et al.*, 2010; *Soret*, 2012]. For example, the nadir observations by VIRTIS as discussed in *Hueso et al.* [2008] exhibit an unexpected region of airglow brightness reaching 7 MR between 60–80°S. Moreover, the time of maximum brightness also varies between 22 h30 and 01 h30 LT [*Hueso et al.*, 2008; *Shakun et al.*, 2010; *Migliorini et al.*, 2011]. This variability in time and location has been attributed to the complex atmospheric circulation on Venus.

[5] For many decades, it has been challenging to model the Venusian O_2 emissions with accuracy because of the uncertainty in both the atmospheric conditions at the altitude of the airglow layer and the kinetic parameters involved in the reaction mechanism producing the emission. Many studies have been focused on the photochemistry using 1-D models [e.g., *Gérard et al.*, 2008a; *Gronoff et al.*, 2008; *Krasnopolsky*, 2010, 2011]. Such an approach addresses one part of the challenge: determining the kinetic parameters. Only recently, 3-D GCMs with self-consistent global-scale dynamics (and various wave processes) of the Martian and Venusian atmospheres, i.e. CO_2-dominated, have begun to be used [*Brecht et al.*, 2011; *Bougher et al.*, 2012; *Clancy et al.*, 2012; *Gagné et al.*, 2012; *Hoshino et al.*, 2012]. In this way, we allow to investigate the uncertainty related to the atmospheric conditions. Modeling of airglow features is a valuable tool for the validation of GCMs to represent realistic atmospheric conditions: the comparison of simulations results with measurements constrains the density profiles of the constituents that are involved in the production mechanisms. The oxygen photochemistry, because of its role in controlling the thermal balance, needs to be well captured to produce temperature fields that are consistent with measurements. At the same time, dynamical features like tides modulate the background atmosphere and therefore play an important role in shaping the airglow features. Certainly, lack of clear knowledge of the photochemical constants involved in the reactions producing the O_2 emissions remains a factor influencing the accuracy of any airglow simulations [*Krasnopolsky*, 2011; *Gagné et al.*, 2012; *Slanger et al.*, 2012].

[6] This study adds to previous work by adopting a 3-D GCM to model Venusian airglow and to exploit consistency with recent measurements to determine the impact of different atmospheric conditions [see *Bougher and Borucki*, 1994]. We investigate the influence of the background atmosphere on the distribution of the O_2 emissions in the Venus atmosphere. We present 3-D simulations of the O_2 airglow features from the IR Atmospheric (0-0) band, focused on nighttime, using atmospheric composition obtained from several run scenarios performed with the Venus Thermospheric GCM (VTGCM) ([*Brecht et al.*, 2011; *Bougher et al.*, 2012] and references therein). It will be shown that using a 3-D GCM to obtain the background atmospheric conditions is a more appropriate approach for providing temporal and spatial variations to the airglow simulations.

2. Model Descriptions

2.1. Atmospheric Model

[7] The VTGCM is a 3-D finite-difference hydrodynamic model of the Venus upper atmosphere [e.g., *Bougher et al.*, 1988] which is based on the National Center for Atmospheric Research (NCAR) terrestrial Thermosphere Ionosphere General Circulation Model (TIGCM). A review is given of the structure, formulation, and processes of the updated VTGCM code, as implemented recently in the revised version of *Brecht et al.* [2011].

[8] Briefly, the VTGCM domain covers a 5 by 5 latitude-longitude grid, with 69 evenly-spaced log-pressure levels in the vertical, extending from approximately ~70 to 200 km. The model solves the time-dependent primitive equations for the neutral upper atmosphere. These primitive equations are solved for steady-state solutions and provide geopotential, vertical motion, temperature, zonal and meridional velocities, and mass mixing ratios of specific species. The VTGCM composition includes major species (CO_2, CO, O, and N_2), minor species (O_2, $N(^4S)$, $N(^2D)$, and NO), and dayside photochemical ions (CO_2^+, O_2^+, O^+, and NO^+). In addition, the VTGCM incorporates nightside profiles of specific chemical trace gas species (Cl, Cl_2, ClCO, ClO, H_2, HCl, HO_2, O_3, OH) from an altitude of 80 km to 130 km [*Krasnopolsky*, 2010]. The latest reaction rates being used in the VTGCM are shown in *Brecht et al.* [2011, Tables 1 and 2].

[9] Parameterized formulations are used for CO_2 15-μm cooling, wave drag, and eddy diffusion by using standard aeronomical formulations. The wave drag (Rayleigh friction) is prescribed asymmetrically in local time in order to mimic the observed upper atmosphere retrograde superrotating zonal (RSZ) winds. The asymmetry is created between the evening and morning terminator winds; evening terminator winds are faster than the morning terminator winds. The prescribed RSZ winds are very weak from 80 km to 110 km, where the O_2 nightglow emission typically occurs, and above 110 km, modest RSZ winds emerge, reaching 60 m s^{-1} above ~130 km [*Brecht et al.*, 2011]. The VTGCM can capture the full range of EUV-UV flux conditions (solar maximum to solar minimum).

[10] The parameters of the VTGCM simulations in this study are given as follows: solar minimum fluxes (F10.7 = 70), a maximum nightside eddy diffusion coefficient of 1.0×10^7 cm^2 s^{-1}, and a wave drag parameter of 0.7×10^{-4} s^{-1}.

2.2. Airglow Model

[11] In this work, the airglow fields are calculated offline using a detailed airglow model that incorporates VTGCM atmospheric fields and calculates the volume emission rate (VER) and total intensity for a given set of conditions. This approach reduces computational time and, based on studies conducted for Earth's atmosphere, [e.g., *Smith et al.*, 2003], it is not expected to impact the results discussed here since O_2 IR airglow in itself does not affect the energy balance directly.

[12] Briefly, the VER can be modeled as the ratio of the production to the loss of an excited species, weighted by

Table 1. Kinetics Parameters Used in the Calculations of the VER for the O_2 IR Atmospheric (0-0) Emission and the Different VTGCM Runs

	Run 1	Run 2
$\alpha(a^1\Delta_g)$	0.75[a]	0.7[b]
K ($cm^6\ s^{-1}$)	2.75×10^{-32} [c]	$2.5 \cdot 3 \times 10^{-33} \cdot (300/T)^{3.25}$ [d]
$\tau(a^1\Delta_g)$ (s)	3800[e]	4460[f]
k_{CO_2} ($cm^3\ s^{-1}$)	2×10^{-20} [g]	10^{-20} [b]
k_O ($cm^3\ s^{-1}$)	2×10^{-16} [g]	2×10^{-16} [g]

[a]*Crisp et al.* [1996]; *Gérard et al.* [2008b].
[b]*Krasnopolsky* [2010].
[c]Value of *Campbell and Gray* [1973] × 2.5; [*Nair et al.*, 1994]; [*Slanger et al.*, 2006].
[d]Value of *Smith and Robertson* [2008] × 2.5; [*Nair et al.*, 1994]; [*Krasnopolsky*, 2011].
[e]*Badger et al.* [1965].
[f]Interpretation of the value of *Lafferty et al.* [1998] by *Krasnopolsky* [2011].
[g]Value recommended by *Sander et al.* [2011].

the lifetime of that species. The VER for the excited O_2, assuming production from the three-body recombination reaction and loss through radiative decay and collisional removal, is here calculated as follows:

$$\epsilon = \frac{\alpha K[O]^2[CO_2]}{1 + \tau k_{CO_2}[CO_2]} \quad (1)$$

where α is the total yield of the excited O_2 state and K is the rate coefficient for the recombination reaction of two oxygen atoms in the presence of CO_2 (a three-body reaction), τ is the lifetime of the excited state by radiative deactivation, and k_{CO_2} is the rate coefficient for the collisional removal (or quenching) of the excited state by CO_2. CO_2 is considered the main quenching species since collisional removal by $O(^3P)$, O_2, N_2, and CO is negligible given the low abundance in the Venus atmosphere of the latter species as compared to that of CO_2, i.e., the quenching factors are negligible. The values to be used for the yield from the three-body reaction and the quenching rate of $a^1\Delta_g$ by CO_2 are still a matter of debate [e.g., *Slanger et al.*, 2008; *Krasnopolsky*, 2011; *Gagné et al.*, 2012].

[13] To investigate the impact of using consistent parameters in the offline airglow model and in the full GCM, two different runs of the VTGCM are used in this paper. We use a VTGCM simulation that represents mean conditions for Venus' upper atmosphere during the Venus Express sampling period [*Brecht et al.*, 2011; *Bougher et al.*, 2012], from which it was determined that with a production yield of 0.75 [*Crisp et al.*, 1996; *Gérard et al.*, 2008b], the three-body recombination rate should be 2.75×10^{-32} $cm^6\ s^{-1}$ (value of *Smith and Robertson* [2008] multiplied by a factor of 2.5 as recommended by *Nair et al.* [1994] for CO_2 as the third body), the lifetime 3800 s (rounded value of *Badger et al.* [1965]), and the CO_2 removal rate 2×10^{-20} $cm^3\ s^{-1}$ value recommended in *Sander et al.* [2011]. This VTGCM simulation will be referred to as run 1. We also use a second VTGCM simulation, referred to as run 2, with the photochemical parameters used in *Krasnopolsky* [2011] and claimed to be the best combination to reproduce the airglow emission in the Mars atmosphere following the sensitivity study of *Gagné et al.* [2012]. These parameters are: 0.7 and $2.5 \cdot 3 \times 10^{-33} \cdot (300/T)^{3.25}$ $cm^6\ s^{-1}$ for the three-body recombination yield and rate coefficient [*Krasnopolsky*, 2010; *Smith and Robertson*, 2008], respectively, 4460 s for the lifetime (value of *Lafferty et al.* [1998] as used in *Krasnopolsky* [2011]), and 10^{-20} $cm^3\ s^{-1}$ for the quenching rate coefficient [*Krasnopolsky*, 2010]. In both runs, we use the laboratory-determined removal rate coefficient by O of 2×10^{-16} cm^3 from *Findlay and Snelling* [1971] and *Leiss et al.* [1978] as recommended by [*Sander et al.*, 2011]. These parameters are listed in Table 1.

[14] The difference between these two VTGCM runs resides in the recombination yield and rate coefficient, the radiative lifetime of the O_2 ($a^1\Delta_g$) state, and the CO_2 quenching rate coefficient used in the chemical scheme of the atmospheric model. These parameters directly affect the balance between the production and loss of $a^1\Delta_g$ in the atmosphere, and hence the overall distribution of the O_x species. In Figure 1, we show the global distribution, as a function of altitude versus latitude at 00:00 LT, of temperature and density of atomic oxygen from run 1 (see Figures 1a and 1c, respectively), as well as the difference in each field between run 1 and run 2 (see Figures 1b and 1d, respectively). We observed that both the temperature and atomic oxygen density fields have a local maximum slightly above 100 km over the equatorial region. We also notice the greatest difference in temperature between run 1 and run 2 near 97 km in altitude. Another local maximum of temperature variation between these two runs is found over the mid-latitudes above 100 km. The density of atomic oxygen is larger in run 1 than in run 2 everywhere in the domain but the difference is more pronounced above 110 km for latitudes beyond 30°N.

[15] As in *Gagné et al.* [2012], the VER profiles are fitted to a Chapman distribution to illustrate some characteristics of the emission layer. The expression of the Chapman equation follows the work of *Cox et al.* [2008], *Cox* [2010], and *Royer et al.* [2010] for a completely mixed atmosphere, i.e. mixing factor of $2S = 1$ as described in *Reed and Chandra* [1975]:

$$\epsilon = \epsilon_{\max} \cdot \exp\left[1 - \frac{z - z_{\max}}{H} - \exp\left(-\frac{z - z_{\max}}{H}\right)\right] \quad (2)$$

where $\epsilon_{\max}$ is the maximum value of the VER in the profile, calculated in $cm^3\ s^{-1}$, $z_{\max}$ is the altitude in km at which this maximum occurs, and H is the e-folding depth in km of the emission layer, or characteristic width of the airglow layer. This method enables the use of these three parameters, i.e. $\epsilon_{\max}$, $z_{\max}$, and H, along with the integrated intensity, I, to make quantitative comparisons with the available observations. Figure 2 gives an example of VER profiles with a fitted Chapman layer for 2.5°N and 00 LT using both VTGCM runs. This time and location correspond to the antisolar point where we would expect the strongest emission, as will be explained in Section 3. We notice that the peak VER ($\epsilon_{\max}$), is larger in run 2, which is a consequence of the larger atomic oxygen density in this run, as compared to run 1.

3. Results

[16] We now present our results for the nighttime O_2 1.27-μm emission using the VTGCM run 1 and run 2 for the background atmosphere, as described in Section 2.1. The latitudinal vs. local time distribution of the total integrated

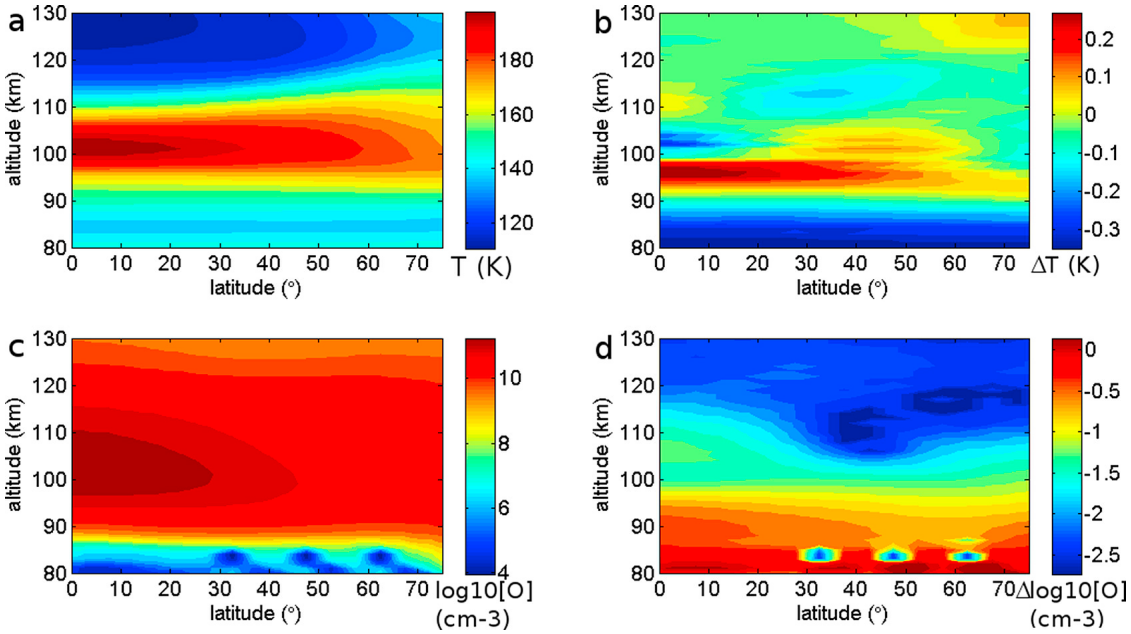

Figure 1. VTGCM results at 00:00 LT as a function of altitude and latitude of: (a) temperature from run 1; (b) absolute difference between run 1 and run 2 temperatures, i.e., T_1–T_2; (c) logarithm of atomic oxygen number density from run 1; and (d) relative difference between run 1 and run 2 logarithms of atomic oxygen, i.e. $([O]_1 - [O]_2)/\{([O]_1 + [O]_2)/2\}$.

intensity from both runs are shown in Figure 3. The maximum integrated intensity is ~1 MR between 00:00 and 01:00 LT around latitude 0°, with the values obtained from the run 2 being slightly larger. The maximum intensity obtained from our calculations is lower than the average maximum brightness of 1.2 MR obtained from observations, as discussed in Section 1. The bright spot location is consistent with the VIRTIS measurements, where it is centered around midnight. In some reports of VIRTIS data, secondary maxima were observed slightly before 00:00 LT or after midnight [*Gérard et al.*, 2008a; *Hueso et al.*, 2008; *Piccioni et al.*, 2009; *Shakun et al.*, 2010; *Migliorini et al.*, 2011; *Soret*, 2012]. The calculated location of the maximum 1.27-μm emission is shifted from midnight as a consequence of relatively weak RSZ winds over the altitude range of the airglow layer in the VTGCM [*Brecht et al.*, 2011], in combination with the relatively long lifetime of $a^1\Delta_g$ at this altitude range, i.e., longer than one hour. Since this emission originates from the three-body recombination of oxygen atoms, it is expected to be maximized near the antisolar point where the oxygen atoms tend to accumulate due to zonal transport caused by the solar to antisolar (SS-AS) circulation followed by vertical transport in the downwelling branch [*Bougher and Borucki*, 1994; *Gérard et al.*, 2009a; *Brecht et al.*, 2011]. The intensity of O_2 in Figure 3 decreases away from the antisolar point, which is consistent with the analyses of *Gérard et al.* [2010] and *Soret et al.* [2011] which show a linear decrease of the limb peak brightness from the antisolar point, i.e., 00 LT, to the terminators, i.e., towards dawn or dusk. Overall, the structure mimics the distribution maps produced with the observations by VIRTIS [*Gérard et al.*, 2008b; *Hueso et al.*, 2008; *Piccioni et al.*, 2009; *Shakun et al.*, 2010; *Soret et al.*, 2011; *Migliorini et al.*, 2011], as well as the atomic oxygen density map near 103 km derived from VIRTIS measurements [*Soret et al.*, 2011] and simulated by the VTGCM [*Brecht et al.*, 2011; *Bougher et al.*, 2012].

[17] The vertical cross sections of the emission rate, i.e., $\epsilon_{\max_i} \cdot \Delta z_i$, as calculated by our model using the atmospheric conditions from the two VTGCM runs are seen is Figure 3.

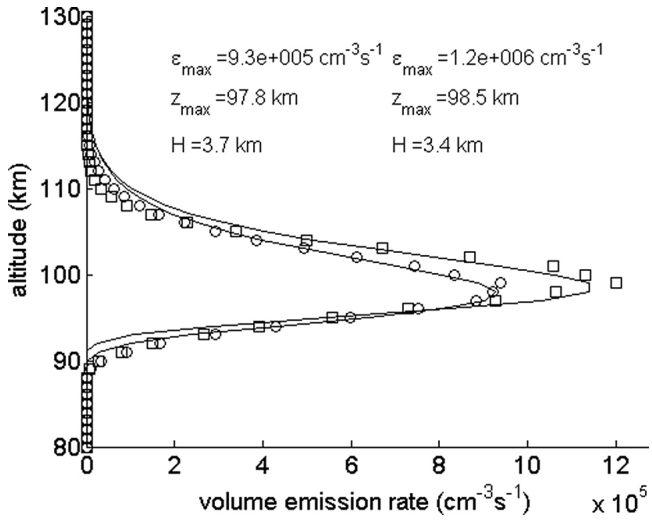

Figure 2. VER (cm^{-3} s^{-1}) profiles calculated with atmospheric conditions from the VTGCM run 1 (squares) and run 2 (circles) at 00:00 LT for latitude 2.5°N as a function of altitude (km). The symbols are the model-calculated values and the lines are the fitted Chapman layer. The parameters of the Chapman fit, i.e., $\epsilon_{\max}$, $z_{\max}$, and H, for each case are given.

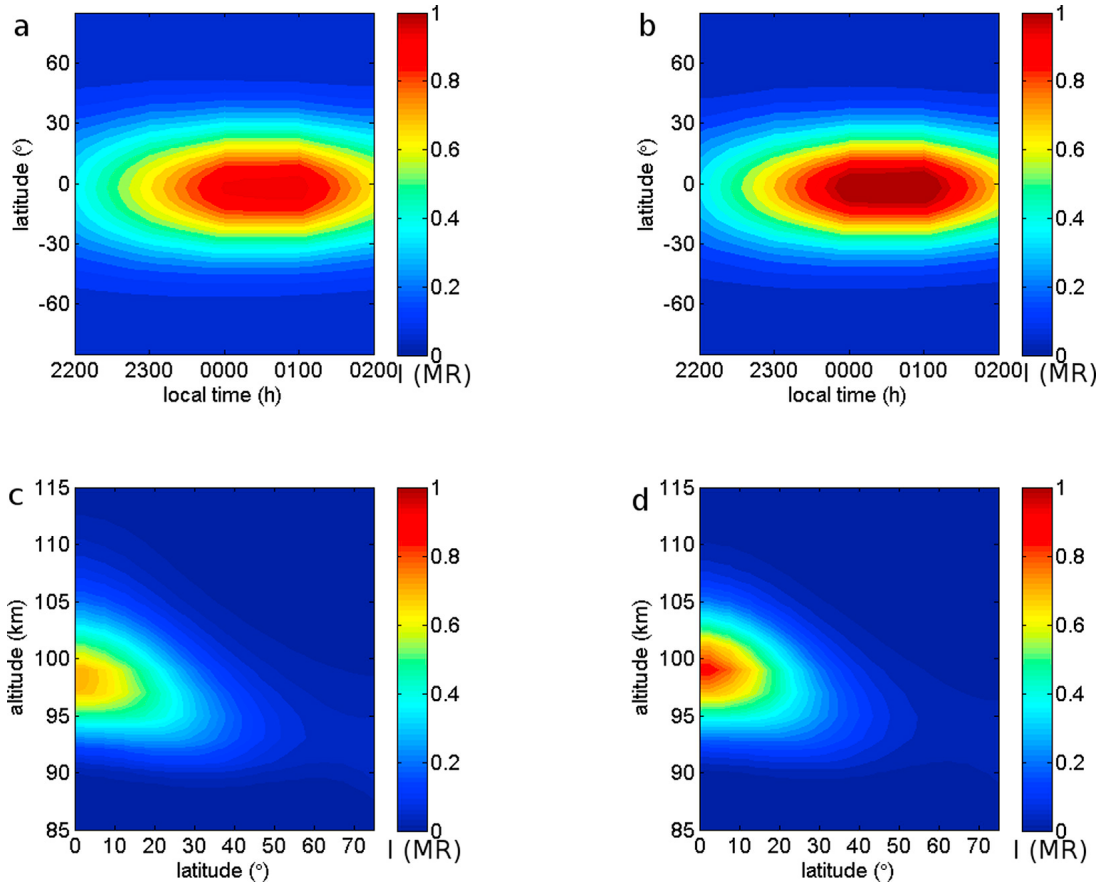

Figure 3. Contours of total integrated intensity (MR) as a function of latitude (°) vs. local time (hr) with the VTGCM (a) run 1 and (b) run 2. Contours of total emission rate (MR) averaged between 22:00 LT and 02:00 LT as a function of altitude (km) vs. latitude (°) with the VTGCM (c) run 1 and (d) run 2.

We observe that the airglow layer is maximized at lower latitudes near 97 km for the results from run 1 (see Figure 3c) and 98 km for the results from run 2 (see Figure 3d), with an nighttime average above 0.5 MR between 0 and 20°N in latitude and between 95 and 102 km in altitude. The emission rate decreases towards the North pole and the altitude of the layer also shows a decreasing trend, which is in agreement with the analysis of *Piccioni et al.* [2009] and *Gérard et al.* [2009b]. We reiterate that this distribution is consistent with the hypothesis for the source of the nighttime O_2 1.27-μm being the recombination of oxygen atoms produced on the dayside and carried to the nightside by the SS-AS circulation followed by a downward transport at the antisolar point [*Hueso et al.*, 2008; *Gérard et al.*, 2008b, 2009a, 2010; *Piccioni et al.*, 2009]. The airglow layer characterizes the altitude where there is an equilibrium between the production and loss of the excited state molecule. However, in *Gérard et al.* [2012] some individual measurement sequences from VIRTIS show a second localized maximum near 50°N which is not reproduced in our model. Similarly, some single orbit observations from *Gérard et al.* [2009b, 2012], *Piccioni et al.* [2009] and *Soret et al.* [2011] show maxima of intensity around 30°N. This dynamically-induced variability is not reproduced in our simulations that rely on climatologically-averaged atmospheric conditions.

[18] Figure 4 presents the latitudinal variations of the peak VER, integrated intensity, peak altitude, and characteristic width averaged over the local time range of our simulations, from 22:00 to 02:00 LT. The model results are compared with observations from VIRTIS, i.e., mean values with 1σ standard deviation error bars, as reported in *Piccioni et al.* [2009], which were gathered mainly in the Northern Hemisphere. We observe that in both modeled cases, the peak VER, i.e., ϵ_{max}, is less than 1×10^6 cm^{-3} s^{-1} at 0° and decreases to less than 1×10^5 cm^{-3} s^{-1} at 50°, where it remains constant poleward (Figure 4a). The behavior of the model results of ϵ_{max} is consistent with the trend in the observations from *Piccioni et al.* [2009] for latitudes <25°, with run 2 calculations being closer to the mean values from the measurements in this latitude range. Over the whole latitude range, the model results show a steeper decrease in ϵ_{max} towards the poles than the VIRTIS data set.

[19] For the integrated intensity in Figure 4b, the agreement between the model results and the observations from VIRTIS at low latitudes is satisfying in terms of latitudinal dependence. When looking at the actual values, we notice that the model results offset the observations by about 30%. Beyond 25° latitude, the model results are diverging from the measurements. Moreover, the latitudinal trend of integrated intensity from VIRTIS measurements in singular orbits as

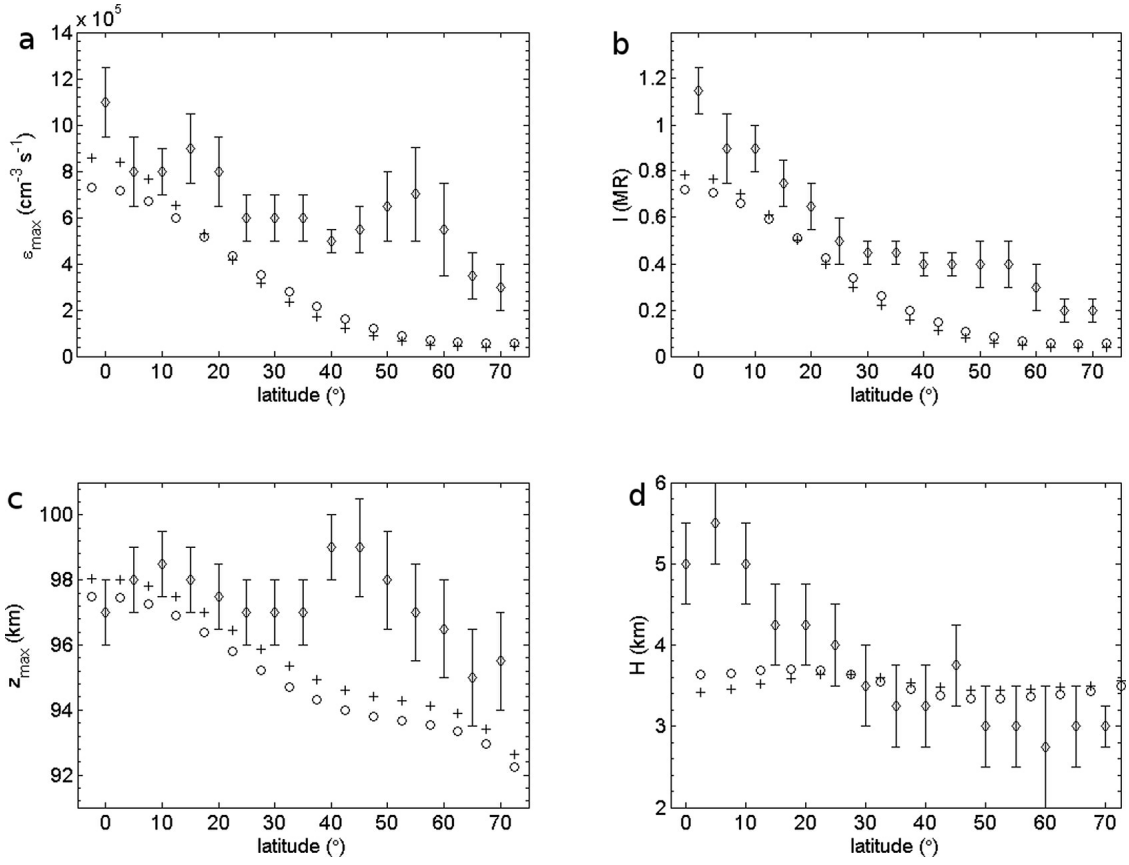

Figure 4. Variations of (a) peak VER (cm^{-3} s^{-1}), (b) intensity (MR), (c) peak altitude (km), and (d) characteristic width (km) with the VTGCM run 1 (circles) and run 2 (pluses) averaged between 22:00 and 02:00 LT as a function of latitude (°). The model results are compared with the observations (diamonds with 1σ error bars) of *Piccioni et al.* [2009] displayed in Figure 6 of that reference. Note that the latter measurements are restricted to the Northern Hemisphere, hence, for consistency, only the results from our model simulations in the Northern Hemisphere are displayed.

reported by *Gérard et al.* [2009a] is sometimes increasing poleward unlike the model results, which consistently decrease poleward.

[20] The peak altitude decreases from 98 km to 94 km between 0° and ∼50° in our simulations using atmospheric conditions from run 2 (Figure 4c), while in *Piccioni et al.* [2009] it oscillates between 97 and 98 km over this latitude range. The peak altitude values of our model are in agreement with the VIRTIS observations, within the error bars for lower latitudes. In *Gérard et al.* [2008b], the peak altitude remains close to 96 km between 17–32°N, in agreement with our calculations. Conversely, the measurements reported from the VIRTIS limb observations by *Gérard et al.* [2010] show a slight increase in peak altitude with latitude by about 2–3 km from 0° to 80°N.

[21] As for the characteristic width, (Figure 4d), in our simulations it is more or less constant throughout the Northern Hemisphere, while *Piccioni et al.* [2009] reported a decreasing trend toward the North Pole for the full width at half maximum (FWHM) of the emission layer, with a steeper rate of decrease between latitudes 0–30°N. The FWHM values from *Piccioni et al.* [2009] have been divided by a factor of 2, i.e., half width at half maximum (HWHM) since HWHM = $z(\epsilon_{max}) - z(\epsilon_{max}/2)$, while the characteristic width is calculated as $H = z(\epsilon_{max}) - z(\epsilon \cdot e^{-1})$, in Figure 4d to provide a more direct comparison with the depth of the airglow layer parameter used in our model. Unlike the previous parameters, the agreement between the modeled H and the measured HWHM, within 1σ standard deviation, is only achieved for latitudes northward of 20°N.

[22] In general, we conclude that with the exception of the characteristic width, the model results from both runs are in agreement with the observations from *Piccioni et al.* [2009] for lower latitudes. For latitudes greater than ∼25°, the simulations results diverge from the mean of the measurements. This behavior is also observed when comparing VTGCM results with O density maps from VIRTIS [*Bougher et al.*, 2012]. Nevertheless, it is important to consider that models yield climatological results from average conditions at specific times and locations while the observations used for comparison in this study are averages of single-point measurements that vary in time and location and can be subject to local variations; variability in the Venus atmosphere is expected.

[23] The agreement in behavior between the airglow simulations using the VTGCM data set representing the VEx-era mean atmospheric conditions, i.e., run 1, and the VEx observations in the equatorial region is encouraging

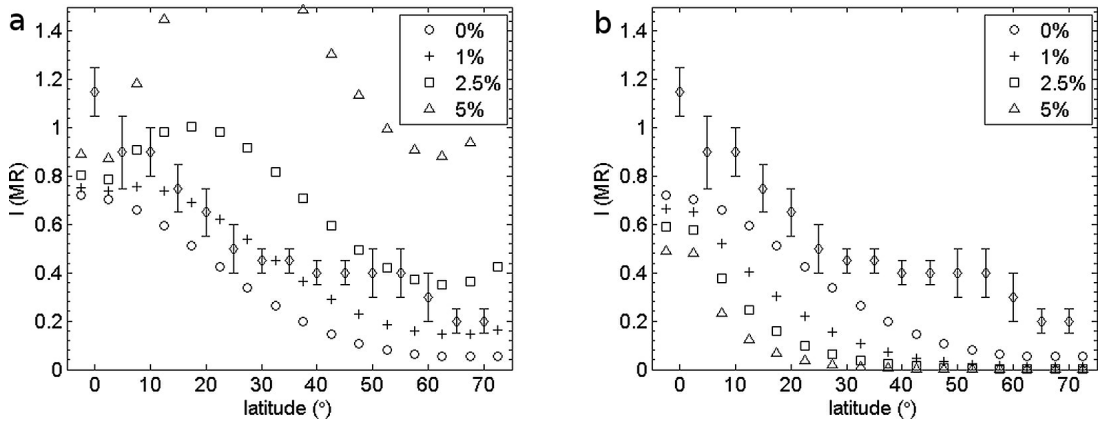

Figure 5. (a) Variations of intensity (MR) as a function of latitude using the VTGCM run 1 averaged between 22:00 and 02:00 LT with an increase in O density as a percentage of increasing latitude by 0% (circles), 1% (pluses), 2.5% (squares), and 5% (triangles). The model results are compared with the observations (diamonds with 1σ error bars) of *Piccioni et al.* [2009, Figure 6]. (b) Same as in Figure 5a but for an increase in temperature as a percentage of increasing latitude.

and gives confidence in the distributions of the species (especially O) and dynamics in the VTGCM. The disagreement at higher latitudes (for peak VER and intensity) is consistent with the findings of *Bougher et al.* [2012], for which the VTGCM-simulated O densities decrease faster with increasing latitude (poleward of 30°) than VEx-extracted O densities [*Soret et al.*, 2011]. The O_2 airglow and atomic O disagreement may come mainly from two sources. First, the VTGCM is designed to produce climatological fields, i.e., mean conditions produced from the tuning of several input parameters as described in Section 2.1, while most of the O_2 IR airglow studies to date use statistically averaged maps of instantaneous emissions and atmospheric conditions from several measurement sequences. Secondly, the transport of O_x species from the equator to the poles may be less efficient, i.e., slower meridional winds, in the VTGCM than actual conditions during the VIRTIS sampling period, as also reported in *Bougher et al.* [2012]. The authors attributed the difference between observed and simulated O density at higher latitudes to the slower wind speeds in the VTGCM at latitudes polewards of 30°, but also to cooler temperatures between 80 km and 90 km. As stated in *Bougher et al.* [2012], Pioneer Venus Orbiter Infrared Radiometer (PV OIR) measurements at 90 km and Venus Express Radio Science (VeRa) occultations show the temperatures increasing from 175 K to 180 from the antisolar point to 60° along the midnight meridian [*Schofield and Taylor*, 1983; *Patzold et al.*, 2007; *Tellmann et al.*, 2009]. However, in Figure 1a, the temperature is 135–145 K between 80–90 km. The cooler temperatures between 80 km and 90 km represent smaller scale heights in this region. From Figure 4d, we can see that indeed the scale heights near the equator are smaller in the model simulations. Also, the scale height is nearly constant for all latitudes, which is representative of the temperature distribution. Near the equator, the dynamics contribute to the oxygen supply, but farther from the equator, the dynamics are not converging, i.e., less pronounced downward transport than at the antisolar point, and the temperature structure below is more evident.

[24] Sensitivity tests have been done by gradually increasing the O density from the equator to the poles, which results in a decrease of the absolute difference between the modeled and observed intensities and VER, but not for the peak altitude and the characteristic width of the airglow layer. The sensitivity to temperature was also assessed with tests done by changing the temperature field in the same way. Figure 5 demonstrates the results from the sensitivity tests on the intensity distribution. We notice that by increasing gradually the oxygen density towards the pole by 2.5%, i.e., $[O] = [O] \cdot (1 + 0.025 \cdot lat)$, the offset between the observed and modeled intensities is minimized (see Figure 5a). However, increasing the temperature did not make the observed and modeled values converge (see Figure 5b). These sensitivity tests therefore strengthen the argument that the O distribution beyond >30° latitude is underestimated in the VTGCM. It is possible that the modeled vertical transport over the polar regions is not as efficient as in the actual Venusian atmosphere, since the difference between the modeled and the measured peak altitudes of the airglow layer were not improved in these tests (not shown). Following the comparison of the VTGCM representation of the O density field with values derived from O_2 IR nightglow measurements by VIRTIS, *Bougher et al.* [2012] concluded that there is a need to improve the local time variations of the wind patterns in the VTGCM. Indeed, in the GCM, between 100 km and 110 km in altitude, lower latitudes have stronger vertical velocities while above 110 km, higher latitudes have stronger vertical velocities; below 100 km, the vertical velocities are very similar for all latitudes.

[25] The airglow simulation using atmospheric conditions from the VTGCM run 2 is only slightly different from the one performed with the VTGCM run 1. The differences in the intensity distribution of the airglow emission from the $a^1\Delta_g$ state between these two sets of simulations (Figure 3), as will be described below, reflect the dependence of the airglow model on the background atmosphere. From simulations of the VER profiles using different atmospheric conditions and several combinations of kinetic parameters (not shown here),

we observed that the profiles converge toward a similar airglow profile when the background state of the atmosphere is carefully chosen, as can be seen from the example given in Figure 2. This convergence of the simulated O_2 airglow profiles is evident when examining the latitudinal variations of the peak VER, integrated intensity, peak altitude, and e-folding depth in Figure 4.

[26] The changes in the kinetic parameters between VTGCM runs 1 and 2 affect the lifetime of atomic oxygen in the middle atmosphere, and therefore induce variations in the atomic oxygen density profile, as shown in Figure 1d. In fact, the effect of dynamics on O_x distributions has been explained in the literature [*Gérard et al.*, 2010; *Brecht et al.*, 2011; *Bougher et al.*, 2012]. Our results confirm that the structure of the airglow layer depends significantly on the background atmosphere, most importantly on the O density and temperature profiles, and that the set of kinetic parameters chosen to reproduce the observations is not the only factor to be taken into account. Indeed, we obtain converging results from the two simulations by using atmospheric conditions from two different VTGCM runs and adjusting the photochemical parameters in the airglow model. Hence, using a 1-D photochemical model to produce a background atmosphere for airglow studies is only a limited approach.

[27] This conclusion strengthens the argument that dynamics play a significant role in the Venus atmosphere. For example, it was shown from modeling studies and observations that the gravity waves affect the background atmosphere and therefore are reflected in the airglow fields [e.g., *Zhang et al.*, 1996; *Bougher et al.*; 1997; *Melo et al.*, 2006; *Piccioni et al.*, 2009]. *Brecht et al.* [2011] studied the sensitivity of the Venusian oxygen density distribution to winds by changing the wave-drag timescale and concluded that the peak density is controlled by this parameter, i.e., stronger winds provide more oxygen atoms on the nightside, resulting in an increased concentration. Moreover, *Hoshino et al.* [2012] advanced the argument that temporal variations of the intensity and distribution in the observations of the O_2 IR emission could be a consequence of Kelvin wave propagation, according to simulations with different planetary wave schemes in their Venus GCM. These dynamical variations cannot be provided by 1-D photochemical models. Lastly, is it well-known that brighter regions of O_2 IR nightglow are correlated with stronger downwelling motion, very often collocated with the antisolar point, i.e. 00 LT and latitude 0° [*Hueso et al.*, 2008; *Gérard et al.*, 2008a, 2009b, 2010; *Shakun et al.*, 2010; *Piccioni et al.*, 2009].

4. Summary

[28] We have investigated the volume emission rate profiles of the O_2 IR Atmospheric emission at 1.27 μm in the Venusian atmosphere using a combination of a Venus GCM and an offline airglow model. We performed airglow simulations using different atmospheric conditions provided by two run scenarios of the VTGCM. We obtained emission rate profiles and airglow intensities that generally match the VIRTIS observations within the range of uncertainty of the measurements. The difference in O distribution between the two VTGCM runs, the results of changing the kinetic parameters in the atmospheric model itself, is sufficient to reproduce the range of airglow observations from VIRTIS. This confirms the fact that O_x distribution relates to both the background atmospheric conditions and the photochemistry.

[29] We showed that using GCM initial conditions that differ in the kinetic parameters used in the oxygen photochemical scheme of the VTGCM, i.e. the three-body rate coefficient and yield, the lifetime, and the CO_2 quenching rate, leads to variations in the atomic oxygen distribution, as expected. Given that the variations in atomic oxygen density directly impact the values of the O_2 airglow peak altitude and emission rate, we adjusted the photochemical parameters in the airglow model to obtain results that were consistent between the two simulations. Hence, this sensitivity study illustrates that differences in the airglow morphology are reduced when we use consistent atmospheric conditions with the observations conditions, hence the choice of photochemical parameters on the airglow structure is not the only determining factor.

[30] Our model study describes the behavior of the peak intensity, peak altitude, and characteristic width of the airglow layer. However, the model forecasts a faster decrease of these parameters towards the poles as compared to the measurements. This model tendency is explained by the O distribution over the poles being under-estimated in the VTGCM, which correlates with colder temperature and a steeper decreasing latitudinal trend, as compared to the VEx-era mean conditions. The weaker meridional transport towards the poles, as the result of the use of Rayleigh friction in the VTGCM, is thought to be the cause to this misrepresentation of the atomic oxygen density [*Bougher et al.*, 2012].

[31] In conclusion, we advise that in order to use airglow measurements together with models to constrain any given value of the kinetic constants for the reactions, and in an effort to overcome the lack of laboratory measurements, we need a 3-D representation of the atmosphere to provide dynamics and global patterns. Although photochemical models are useful for local in-depth studies, relying on this type of model to reproduce airglow observations is not recommended since these models limit the dynamical variations and may not capture the actual distribution of constituents. Furthermore, another modeling improvement would be to combine kinetic and/or fluid approaches, as is done in 1-D photochemical modeling studies, with 3-D GCMs as inputs, hence bridging the gaps between these two methods.

[32] **Acknowledgments.** The authors are grateful to Giuseppe Piccioni for the useful exchanges and help regarding the interpretation of the VIRTIS data. The authors would like to acknowledge the Fonds Québécois de la Recherche sur la Nature et les Technologies, the Natural Sciences and Engineering Research Council of Canada, and the Canadian Space Agency for funding. They would also like to acknowledge NASA (grant NNX08AG18G) for supporting this research at the University of Michigan.

References

Badger, R. M., A. C. Wright, and R. F. Whitlock (1965), Absolute intensities of discrete and continuous absorption bands of oxygen gas at 1.26 and 1.065 μm and radiative lifetime of $^1\Delta_g$ state of oxygen, *J. Chem. Phys.*, *43*(12), 4345–4350.

Bailey, J., V. S. Meadows, S. Chamberlain, and D. Crisp (2008), The temperature of the Venus mesosphere from O_2 ($a^1\Delta_g$) airglow observations, *Icarus*, *197*(1), 247–259.

Bougher, S. W., and W. J. Borucki (1994), Venus O_2 visible and IR nightglow: Implications for lower thermosphere dynamics and chemistry, *J. Geophys. Res.*, *99*(E2), 3759–3776.

Bougher, S. W., R. E. Dickinson, E. C. Ridley, and R. G. Roble (1988), Venus mesosphere and thermosphere: III. Three-dimensional general-circulation with coupled dynamics and composition, *Icarus*, *73*(3), 545–573.

Bougher, S. W., M. J. Alexander, and H. G. Mayr (1997), Upper atmosphere dynamics: Global circulation and gravity waves, in *Venus II: Geology, Geophysics, Atmosphere, and Solar Wind Environment*, pp. 259–291, Univ. of Ariz., Tucson.

Bougher, S. W., S. Rafkin, and P. Drossart (2006), Dynamics of the Venus upper atmosphere: Outstanding problems and new constraints expected from Venus Express, *Planet. Space Sci.*, *54*(13–14), 1371–1380.

Bougher, S. W., J.-C. Gérard, L. Soret, and A. S. Brecht (2012), Atomic oxygen distributions in the Venus thermosphere: Comparisons between Venus Express observations and global model simulations, *Icarus*, *217*(2), 759–766.

Brecht, A. S., S. W. Bougher, J. C. Gerard, C. D. Parkinson, S. Rafkin, and B. Foster (2011), Understanding the variability of nightside temperatures, NO UV and O_2 IR nightglow emissions in the Venus upper atmosphere, *J. Geophys. Res.*, *116*, E08004, doi:10.1029/2010JE003770.

Campbell, I. M., and C. N. Gray (1973), Rate constants for $O(^3P)$ recombination and association with $N(^4S)$, *Chem. Phys. Lett.*, *18*(4), 607–609.

Clancy, R. T., et al. (2012), Extensive MRO CRISM observations of 1.27 μm O_2 singlet delta airglow in Mars polar night and their comparison to MRO MCS temperature profiles and LMD GCM simulations, *J. Geophys. Res.*, *117*, E00J10, doi:10.1029/2011JE004018.

Connes, P., J. F. Noxon, W. A. Traub, and N. P. Carleton (1979), $O_2(^1\Delta)$ emission in the day and night airglow of Venus, *Astrophys. J.*, *233*(1), L29–L32.

Cox, C. (2010), Analyse et modélisation des émissions ultraviolettes de l'atmosphère de Vénus et de Mars à l'aide des instruments SPICAM et SPICAV, PhD thesis, Université de Liège, Liège, Belgium.

Cox, C., A. Saglam, J.-C. Gérard, J.-L. Bertaux, F. González-Galindo, F. Leblanc, and A. Reberac (2008), Distribution of the ultraviolet nitric oxide Martian night airglow: Observations from Mars Express and comparisons with a one-dimensional model, *J. Geophys. Res.*, *113*, E08012, doi:10.1029/2007JE003037.

Crisp, D., V. S. Meadows, B. Bézard, C. deBergh, J. P. Maillard, and F. P. Mills (1996), Ground-based near-infrared observations of the Venus nightside: 1.27-μm $O_2(a^1\Delta_g)$ airglow from the upper atmosphere, *J. Geophys. Res.*, *101*,(E2), 4577–4593, doi:10.1029/95JE03136.

Findlay, F. D., and D. R. Snelling (1971), Collisional deactivation of $O_2(^1\Delta_g)$, *J. Chem. Phys.*, *55*(2), 545–551.

Gagné, M.-E., S. M. L. Melo, F. Lefèvre, F. González-Galindo, and K. Strong (2012), Modeled O_2 airglow distribution in the Martian atmosphere, *J. Geophys. Res.*, *117*, E06005, doi:10.1029/2011JE003901.

García Muñoz, A., F. P. Mills, T. G. Slanger, G. Piccioni, and P. Drossart (2009), Visible and near-infrared nightglow of molecular oxygen in the atmosphere of Venus, *J. Geophys. Res.*, *114*, E12002, doi:10.1029/2009JE003447.

Gérard, J.-C., B. Hubert, V. I. Shematovich, D. V. Bisikalo, and G. R. Gladstone (2008a), The Venus ultraviolet oxygen dayglow and aurora: Model comparison with observations, *Planet. Space Sci.*, *56*(3–4), 542–552.

Gérard, J.-C., A. Saglam, G. Piccioni, P. Drossart, C. Cox, S. Erard, R. Hueso, and A. Sanchez-Lavega (2008b), Distribution of the O_2 infrared nightglow observed with VIRTIS on board Venus Express, *Geophys. Res. Lett.*, *35*, L02207, doi:10.1029/2007GL032021.

Gérard, J.-C., C. Cox, L. Soret, A. Saglam, G. Piccioni, J.-L. Bertaux, and P. Drossart (2009a), Concurrent observations of the ultraviolet nitric oxide and infrared O_2 nightglow emissions with Venus Express, *J. Geophys. Res.*, *114*, E00B44, doi:10.1029/2009JE003371.

Gérard, J.-C., A. Saglam, G. Piccioni, P. Drossart, F. Montmessin, and J.-L. Bertaux (2009b), Atomic oxygen distribution in the Venus mesosphere from observations of O_2 infrared airglow by VIRTIS-Venus Express, *Icarus*, *199*(2), 264–272.

Gérard, J.-C., L. Soret, A. Saglam, G. Piccioni, and P. Drossart (2010), The distributions of the OH Meinel and $O_2(a^1\Delta_g\text{-}X^3\Sigma)$ nightglow emissions in the Venus mesosphere based on VIRTIS observations, *Adv. Space Res.*, *45*(10), 1268–1275.

Gérard, J.-C., F. Montmessin, G. Piccioni, P. Drossart, J.-L. Bertaux, L. Soret (2012), Spatial correlation of OH Meinel and O_2 infrared atmospheric nightglow emissions observed with VIRTIS-M on board Venus Express, *Icarus*, *217*(2), 813–817.

Gronoff, G., J. Lilensten, C. Simon, M. Barthelemy, F. Leblanc, and O. Dutuit (2008), Modelling the Venusian airglow, *Astron. Astrophys.*, *48*(3), 1015–1029.

Hoshino, N., H. Fujiwara, M. Takagi, Y. Takahashi, and Y. Kasaba (2012), Characteristics of planetary-scale waves simulated by a new venusian mesosphere and thermosphere general circulation model, *Icarus*, *217*(2), 818–830.

Hueso, R., A. Sanchez-Lavega, G. Piccioni, P. Drossart, J.-C. Gérard, I. Khatuntsev, L. Zasova, and A. Migliorini (2008), Morphology and dynamics of Venus oxygen airglow from Venus Express/Visible and Infrared Thermal Imaging Spectrometer observations, *J. Geophys. Res.*, *113*, E00B02, doi:10.1029/2008JE003081.

Krasnopolsky, V. A. (2010), Venus night airglow: Ground-based detection of OH, observations of O_2 emissions, and photochemical model, *Icarus*, *207*(1), 17–27.

Krasnopolsky, V. A. (2011), Excitation of the oxygen nightglow on the terrestrial planets, *Planet. Space Sci.*, *59*(8), 754–766.

Lafferty, W. J., A. M. Solodov, C. L. Lugez, and G. T. Fraser (1998), Rotational line strengths and self-pressure-broadening coefficients for the 1.27-μm, $a^1\Delta_g\text{-}X^3\Sigma_g^-$, $v = 0\text{-}0$ band of O_2, *Appl. Opt.*, *37*(12), 2264–2270.

Leiss, A., U. Schurath, K. H. Becker, and E. H. Fink (1978), Revised quenching rate constants for metastable oxygen molecules $O2(a^1\Delta_g)$, *J. Photochem.*, *8*(3), 211–214.

Melo, S. M. L., O. Chiu, A. García Muñoz, K. Strong, J. C. McConnell, T. G. Slanger, M. J. Taylor, R. P. Lowe, I. C. McDade, and D. L. Huestis (2006), Using airglow measurements to observe gravity waves in the Martian atmosphere, *Adv. Space Res.*, *38*(4), 730–738.

Migliorini, A., et al. (2011), Oxygen airglow emission on Venus and Mars as seen by VIRTIS/VEX and OMEGA/MEX imaging spectrometers, *Planet. Space Sci.*, *59*(10), 981–987.

Nair, H., M. Allen, A. D. Anbar, Y. L. Yung, and R. T. Clancy (1994), A photochemical model of the Martian atmosphere, *Icarus*, *111*(1), 124–150.

Ohtsuki, S., N. Iwagami, H. Sagawa, Y. Kasaba, M. Ueno, and T. Imamura (2005), Ground-based observation of the Venus 1.27-μm O_2 airglow, *Planet. Atmos. Ionos. Magn.*, *36*(11), 2038–2042.

Ohtsuki, S., N. Iwagami, H. Sagawa, M. Ueno, Y. Kasaba, T. Imamura, K. Yanagisawa, and E. Nishihara (2008), Distributions of the Venus 1.27-μm O_2 airglow and rotational temperature, *Planet. Space Sci.*, *56*(10), 1391–1398.

Patzold, M., et al. (2007), The structure of Venus' middle atmosphere and ionosphere, *Nature*, *450*, 657–660.

Piccioni, G., L. Zasova, A. Migliorini, P. Drossart, A. Shakun, A. García Muñoz, F. P. Mills, and A. Cardesin-Moinelo (2009), Near-IR oxygen nightglow observed by VIRTIS in the Venus upper atmosphere, *J. Geophys. Res.*, *114*, E00B38, doi:10.1029/2008JE003133.

Reed, E. I., and S. Chandra (1975), Global characteristics of atmospheric emissions in lower thermosphere and their aeronomic implications, *J. Geophys. Res.*, *80*(22), 3053–3062.

Royer, E., F. Montmessin, and J.-L. Bertaux (2010), NO emissions as observed by SPICAV during stellar occultations, *Planet. Space Sci.*, *58*(10), 1314–1326.

Sander, S. P., et al. (2011), Chemical kinetics and photochemical data for use in atmospheric studies, *Tech. Rep. 15*, Jet Propulsion Lab., Pasadena, Calif.

Schofield, J. T., and F. W. Taylor (1983), Measurements of the mean, solar-fixed temperature and cloud structure of the middle atmosphere of Venus, *Q. J. R. Meteorol. Soc.*, *109*(459), 57–80.

Shakun, A. V., L. V. Zasova, G. Piccioni, P. Drossart, and A. Migliorini (2010), Investigation of oxygen $O_2(a^1\Delta_g)$ emission on the nightside of Venus: Nadir data of the VIRTIS-M experiment of the Venus Express mission, *Cosmic Res.*, *48*(3), 232–239.

Slanger, T. G., D. L. Huestis, P. C. Cosby, N. J. Chanover, and T. A. Bida (2006), The Venus nightglow: Ground-based observations and chemical mechanisms, *Icarus*, *182*(1),1–9.

Slanger, T. G., T. E. Cravens, J. Crovisier, S. Miller, and D. F. Strobel (2008), Photoemission phenomena in the solar system, *Space Sci. Rev.*, *139*, 267–310.

Slanger, T. G., N. J. Chanover, B. D. Sharpee, and T. A. Bida (2012), O/O_2 emissions in the Venus nightglow, *Icarus*, *217*(2), 845–848.

Smith, A. K., D. R. Marsh, and A. C. Szymczak (2003), Interaction of chemical heating and the diurnal tide in the mesosphere, *J. Geophys. Res.*, *108*(D5), 4164, doi:10.1029/2002JD002664.

Smith, G. P., and R. Robertson (2008), Temperature dependence of oxygen atom recombination in nitrogen after ozone photolysis, *Chem. Phys. Lett.*, *458*(1–3), 6–10.

Soret, L., J.-C. Gérard, G. Piccioni, and P. Drossart (2011), The OH Venus nightglow: morphology and relation to ozone in the upper atmosphere paper presented at Joint Meeting 2011, Eur. Planet. Sci. Congress and Div. for Planet. Sci of the Am. Astron. Soc., Nantes, France.

Soret, L., G. Piccioni, P. Drossart, J.-C. Gérard (2012), Atomic oxygen on the Venus nightside: Global distribution deduced from airglow mapping, *Icarus*, *217*(2), 849–855.

Tellmann, S., M. Päetzold, B. Häeusler, M. K. Bird, and G. L. Tyler (2009), Structure of the Venus neutral atmosphere as observed by the Radio Science experiment VeRa on Venus Express, *J. Geophys. Res.*, *114*, E00B36, doi:10.1029/2008JE003204.

Zhang, S., S. W. Bougher, and M. J. Alexander (1996), The impact of gravity waves on the Venus thermosphere and O_2 IR nightglow, *J. Geophys. Res.*, *101*(E10), 23,195–23,205.